



Effect of the Distance from Build Platform and Post-Heat Treatment of AlSi10Mg Alloy Manufactured by Single- and Multi-Laser Selective Laser Melting

Emanuela Cerri, Emanuele Ghio, and Giovanni Bolelli

Submitted: 24 November 2020 / Revised: 29 January 2021 / Accepted: 6 February 2021 / Published online: 17 March 2021

In the present study, AlSi10Mg samples produced by selective laser melting (SLM) were studied. Samples were machined from two types of bars obtained through different methods: either single laser (SL) or multiple laser (ML) machine setup. The bars were built perpendicular to the platform, which was pre-heated at 150 °C (working temperature), up to a height of 300 mm. The effect of the distance from the platform on the mechanical properties was investigated through tensile samples in as-built condition and after unconventional heat treatments (U-HT). Tensile strength changed by 80 MPa along the Z-axis (build direction) for SL case and by 100 MPa for ML case in the as-built samples. Vickers microhardness revealed an analogous gradient. This was correlated to a gradient in intra-granular precipitates' distribution along the Z-axis, as revealed by scanning electron microscopy (SEM). An unconventional heat treatment at 175 °C for 6h slightly improves the mechanical strength; higher temperature treatments at 200 and 225 °C for the same duration cause a progressive decrease in strength with an increase in elongation. The amount and size of the precipitates and the thickness of eutectic Si change with the heat treatment temperature, justifying the mechanical behavior.

Keywords AlSi10Mg, build axis, mechanical properties, selective laser melting

1. Introduction

Selective laser melting (SLM) is a particular additive manufacturing (AM) process that allows producing metal components of complex geometry. The most frequently used materials, known for returning excellent properties after SLM processing, are aluminum alloys, titanium alloys, steel, Inconel (Ref 1, 2). Usually, SLMed alloys exhibit higher tensile strength and microhardness than their as-cast counterparts due to the optimization of laser scan speed, scan strategy, build direction and new heat treatments (Ref 3, 4). In this context,

improve not only the efficiency of aluminum alloy, but also the build rate compared to single laser (Ref 5, 6).

As reported by A.H. Maamoun et al. (Ref 7) and K.G. Prashanth et al. (Ref 8), the eutectic unstable microstructure of AlSi10Mg produced by SLM affects their mechanical properties. Specifically, the SLM technology kinetically promotes a cellular microstructure: the part of liquid remaining after α -Al solidification generates the formation of eutectic Si along the cellular boundaries during the molten pool solidification. Considering the scan strategy of SLM, it is possible to observe that various laser passes induce a microstructural variation: in fact, a heat-affected zone is generated at the edge of any part of the material that has been melted (Ref 7–9). The same morphological inhomogeneity is also present along the Z-axis as reported by (Ref 3, 8, 9), and in the case of overlapping lasers there is a condition of inhomogeneity within molten pools (Ref 7, 10). However, a variation of mechanical properties is also present along the Z-axis or build axis (Ref 2, 4, 11, 12).

Moreover, the conditions of molten pool solidification such as the high cooling rate (10^6 K/s) and the variation of solubility of Si in the Al matrix (Ref 8) make the cellular microstructure very sensitive to a limited increase in temperature, for example, through an aging heat treatment at low temperature (~ 200 °C) (Ref 8, 13, 14).

Due to this sensitivity, the pre-heated build platform may influence the detectable gradient of mechanical properties as a function of distance from the surface. As reported by Brandl et al. (Ref 10), the presence of a pre-heated platform induces an increase in mechanical properties. As matter of fact, the permanence of the samples in the temperature range between 150 °C and 200 °C causes the precipitation of an extremely fine Mg₂Si phase along the boundary of cellular α -Al. Several studies have shown the coexistence of Mg and Si in the same region around the α -Al grains (Ref 7–9).

This invited article is part of a special topical focus in the Journal of Materials Engineering and Performance on Additive Manufacturing. The issue was organized by Dr. William Frazier, Pilgrim Consulting, LLC; Mr. Rick Russell, NASA; Dr. Yan Lu, NIST; Dr. Brandon D. Ribic, America Makes; and Caroline Vail, NSWC Carderock.

Emanuela Cerri and **Emanuele Ghio**, Department of Engineering and Architecture, University of Parma, Via G. Usberti 181/A, 43124 Parma, Italy; **Giovanni Bolelli**, Department of Engineering “Enzo Ferrari”, University of Modena and Reggio Emilia, Via Pietro Vivarelli 10/1, 41125 Modena, Italy; InterMech – MO.RE. Centro Interdipartimentale per la Ricerca Applicata e i Servizi nel Settore della Meccanica Avanzata e della Motoristica, Università di Modena e Reggio Emilia, Via Pietro Vivarelli 2, 41125 Modena, Italy; and Consorzio Interuniversitario Nazionale per la Scienza e Tecnologia dei Materiali (INSTM), Local Unit, Università di Modena e Reggio Emilia, Via Pietro Vivarelli 10/1, 41125 Modena, Italy. Contact e-mails: emanuela.cerri@unipr.it and emanuele.ghio@unipr.it.

Interesting results are also obtained by aging the AlSi10Mg alloy; in fact, the applied heat treatments induced a coarsening of eutectic Si and the precipitation of Mg₂Si phase, in addition to a homogenization of the microstructure, a reduction of porosity and an increase in ductility (Ref 2, 3, 15, 16, 17). Takata et al. (Ref 17) demonstrated the greater presence of Mg₂Si at temperatures below 400 °C. On the other hand, Lam et al. (Ref 9) and Li et al. (Ref 16) showed the presence of Mg₂Si precipitates even within as-built samples. The thermal cycles induced by SLM technology led to diffusion of Mg and Si atoms through quenched-in vacancies within the α -Al supersaturated matrix and consequently to the formation of Mg₂Si phase on preferential sites (Ref 18) such as dislocations (Ref 19). If a solution heat treatment (SHT) is applied (Ref 3, 7), a significant coarsening of the microstructure and a destruction of eutectic Si network are induced, causing a decrease in UTS and σ_y .

In the same scenario, an unconventional heat treatment without SHT can be considered with the aim to prevent an excessive decrease in strength while increasing the ductility as reported by Montero et al. (Ref 20). In conclusion, Fiocchi et al. (Ref 14) used low aging temperatures and demonstrated a significant decrease in mechanical properties already at 294 °C.

In the current scenario, this paper aims to investigate the mechanical properties and microstructure of the AlSi10Mg SLM alloy as function of the distance along the build axis in as-built and in unconventional heat treatment conditions. The samples printed with single laser and multi-laser are analyzed in as-built condition. The obtained results show a slight different between single laser and multi-laser, so the only single laser samples are studied for the different heat treatment conditions.

2. Materials and Methods

Bulk specimens of AlSi10Mg aluminum alloy were produced by SLM from spherical gas-atomized powder with nominal composition as shown in Table 1. SLM processing was carried out at 150 °C using an SLM500 device (quad laser SLM solutions) equipped with an Yb:YAG laser. The parameters used for preparing the samples are as follows: scanning speed 1500 mm/s, power 350 W, layer thickness 50 μ m, hatch spacing 0.17 mm. High purity argon gas was used during SLM processing in order to avoid oxygen contamination. Two different bars (300x100x10 mm) are manufactured by single laser (SL) and multi-laser (ML), respectively, in zones D and AB of pre-heated build platform (Fig. 1a). In agreement of ASTM E804 standard (Fig. 1b), 26 tensile samples have been machined to machine tools for each bar printed. Moreover, the axis of symmetry of these samples was kept parallel to build platform as reported in (Fig. 1a).

The build pre-heated platform is divided in two different zones: the first bar (D) is produced by single laser, while the second, bar (AB), is produced by quadruple laser delivered

though specific algorithms created by the SLM500 machine manufacturer. Moreover, “top” was used to designate samples cut at bar height > 150 mm and “bottom” for samples extracted at bar height < 150 mm.

The AlSi10Mg samples were subjected to different unconventional heat treatments at 175 °C (U-HT1), 200 °C (U-HT2) and 225 °C (U-HT3) up to 6h, performed in a muffle furnace (Nabertherm) with the K-thermocouple placed in contact to samples.

For tensile tests, samples in as-built and unconventional heat treated conditions were cut and machined from the solid geometries (Fig. 1b), according to ASTM E804. Tensile tests were performed at room temperature using a Zwick Z100 servo hydraulic device, at a strain rate of 0.008 s⁻¹.

Vickers microhardness was measured at different heights (in the vertical bars shown in Figure 1a) and in all different thermal treatment conditions by 500 gf load and a dwell time of 15s.

For microstructure investigations, samples were mechanically ground with SiC papers and polished using colloidal silica suspension (\approx 60 nm size). Microstructure was characterized by

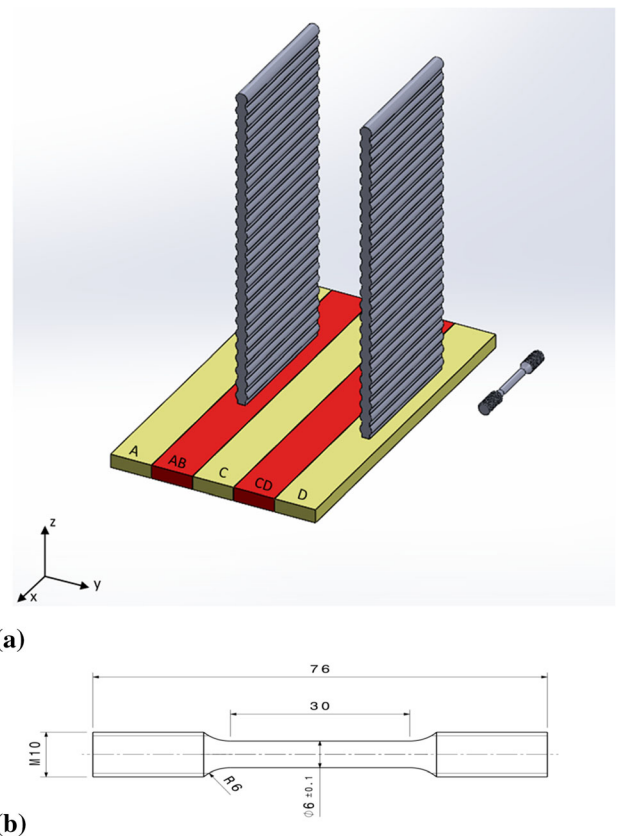


Fig. 1 (a) Bar AB (ML) and bar D (SL) produced by SLM. Tensile sample machined by bars with axis of symmetry parallel to build platform; (b) tensile sample according to ASTM E804

Table 1 AlSi10Mg chemical composition (wt.%)

Al	Si	Fe	Mg	Cu	Mn	Zn	Ti	Pb	Sn
Bal.	9.60	0.10	0.38	< 0.05	< 0.01	< 0.01	< 0.01	< 0.01	< 0.01

optical microscope (OM) (Leica DMi8) and scanning electron microscopy (SEM: Nova NanoSEM 450 equipped with a field emission gun source, FEI Thermo Fisher Scientific, Hillsboro, Oregon, USA). Phase composition was assessed by x-ray diffraction (XRD: X'Pert PRO, PANALytical, Almelo, NL) using Cu-K α radiation emitted from a conventional source operated at 40 kV, 40 mA and detected through a 1D array of solid-state detectors (XCelerator, PANALytical) with a Ni filter.

Finally, statistical analysis of porosity dimension and eutectic Si band thickness was performed on polished sample sections by image analysis (LAS image software equipped with the OM).

3. Result and Discussion

3.1 Microstructure and Mechanical Properties of as-Built AlSi10Mg Samples

Figure 2 shows the fine and inhomogeneous microstructure of SLM samples analyzed in the XY plane and in the XZ plane. As widely reported in the literature, the first plane mentioned is characterized by the characteristic ellipsoidal shapes of molten pool, elongated in the scanning direction; the second shows a “fish scale” structure along build direction. In the next layer, the laser scanning direction is rotated by 90°, as confirmed by the transversal line perpendicular to melt pools. Figure 2(a) and (b) shows the differences between the single laser case (Fig. 2a, D bar) and the multi-laser case (Fig. 2b, AB bar) in XY plane: it

is possible to observe the greater number of different scan track directions in Fig. 2(b). In addition, all micrographs (Fig. 2) are characterized by the random presence of spherical pores that will be discussed later, but in Fig. 2(c) a keyhole pore is showed and it is located between two scan tracks at the edge of molten pool. The microstructure of molten pool (Fig. 3) is characterized by an increase in cell size from the center to the boundary, as widely reported in the literature. Considering the three SEM pictures showing the Fig. 3(b, c, d) (areas 1, 2 and 3 in Fig. 3), the eutectic Si network is gradually destroyed from the center to the coarse and heat-affected zones (HAZ) (Ref 21, 22).

Figure 4 shows the molten pool boundary and the overlap region among two adjacent track scans, which increases if the hatch distance decreases (Ref 22, 23). In this case of study, the sample was scanned with long bidirectional vectors in one layer with a hatch distance of 170 μm . On the other hand, considering the high magnification micrograph shown in Fig. 4(b), it can be emphasized the effect of temperature gradient (G) and the crystal growth rate (R) within the molten pool: the grains growth takes place along the thermal gradient and their orientations change within the molten pool because the G direction varies (Ref 5, 15, 24–26). As matter of fact, from the bottom of molten pool, the G direction remains perpendicular to its boundary; on the contrary, the G direction will be deflected toward the center of the melt pool from the side of the same boundary (Ref 25). In fact, the cross section of molten pool is mainly composed of columnar grains and by small equiaxed grains near melt pool boundary. In the same context, considering a melt pool in the last scanned layer n, the

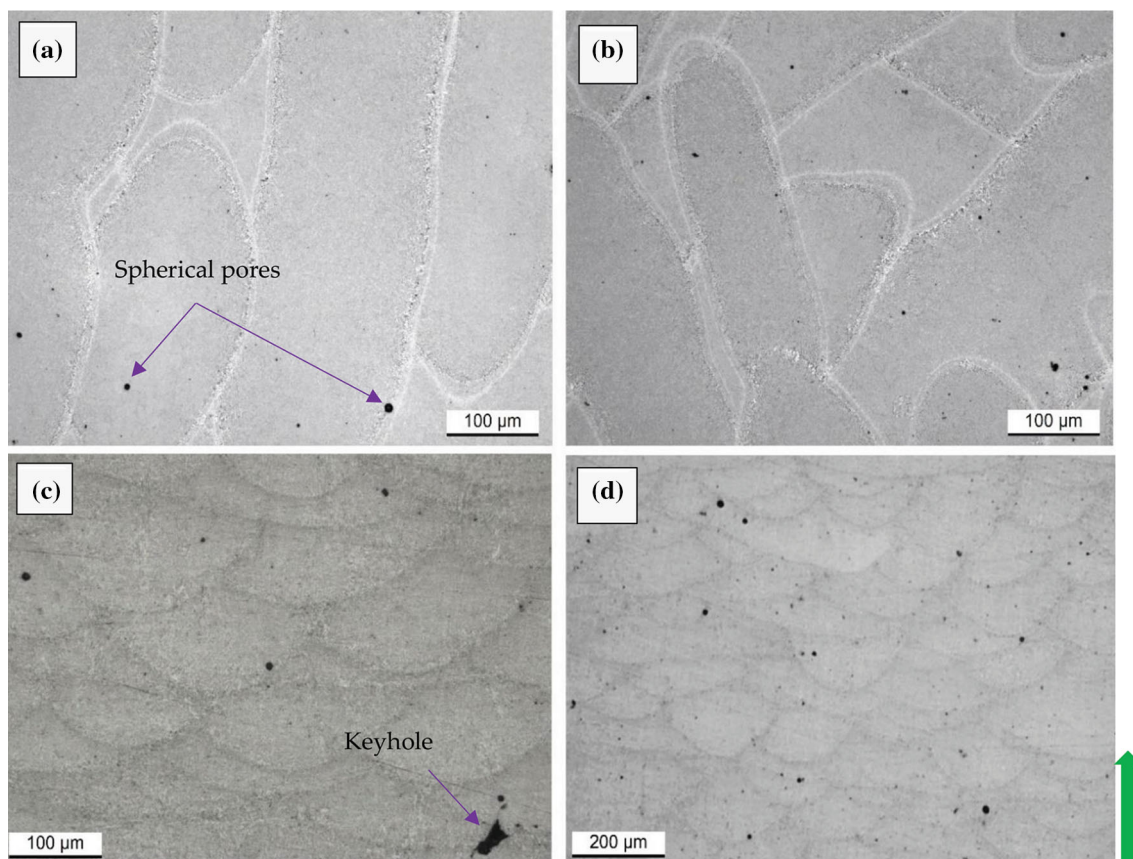


Fig. 2 Light microscopy of SLMed samples showing melt pools, scan tracks and porosity for SL samples (a, c) and ML samples (b, d), respectively, in XY and XZ planes. The green arrow shows the build direction in the XZ plane (Color figure online)

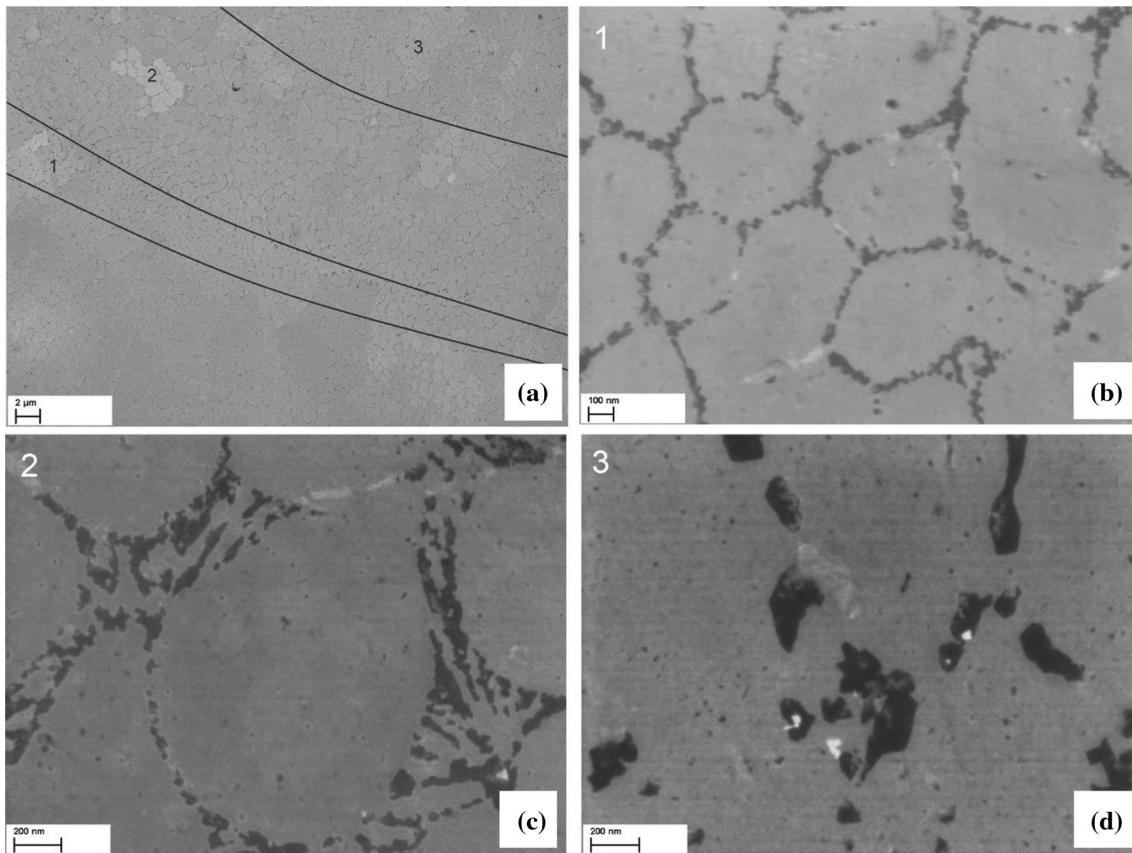


Fig. 3 SEM micrographs of AlSi10Mg sample in as-built condition: (a) molten pool at low magnification (8kX); (b) center of molten pool; (c) coarse zone; (d) HAZ zone

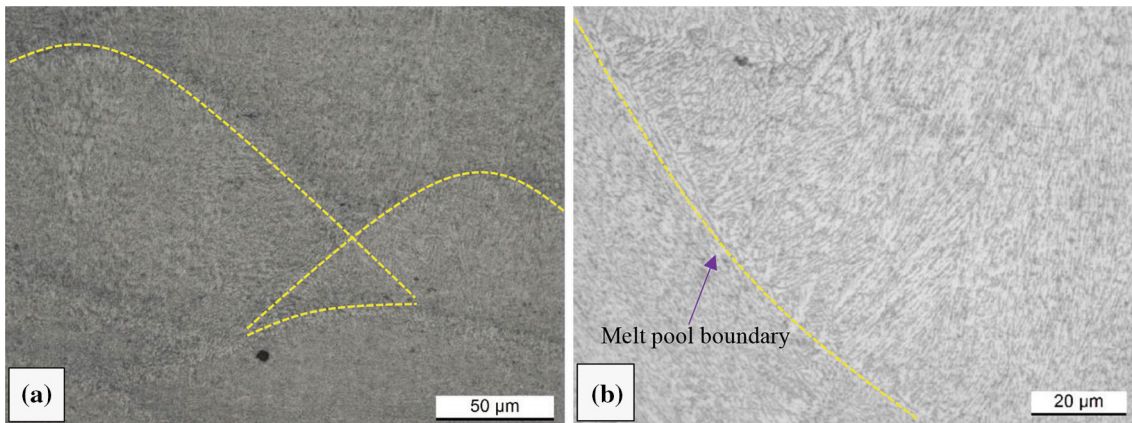


Fig. 4 High magnification micrographs (500x, 1000x) of SLMed samples in as-built condition along the XZ plane: (a) edges of the molten pools (yellow dotted lines) and overlap zone between two track scans; (b) region near fusion line, showing cellular growth (Color figure online)

grains direction can change from 0° to 90° compared to that which characterized the melt pool in the layer $n-1$ (Fig. 4b), as reported by D. Kong et al. (Ref 26). Finally, the characterization of this cellular structure can be done considering the G/R ratio and the product of G and R: the morphology and the size of solidification structure were described by the first and the second values, respectively, as reported by (Ref 25–28).

Image analysis results in Fig. 5(a) shows that the bottom part of the multi-laser case (AB-bottom) has 60% of its porosity

characterized by an equivalent diameter smaller than $1\ \mu\text{m}$, about 17% has a size ranging between 1 and $2\ \mu\text{m}$ and about 7% is between 2 and $3\ \mu\text{m}$, decreasing to zero for larger areas. The overall density is 99.9% on average. At the top of the same bar (i.e., approximately at the maximum distance from the pre-heated platform surface), porosity presents a similar size distribution: 40% of the porosity has an area smaller than $1\ \mu\text{m}$, about 20% between 1 and $2\ \mu\text{m}$ and 15% ranges between 2 and $3\ \mu\text{m}$. The density is 99.2%.

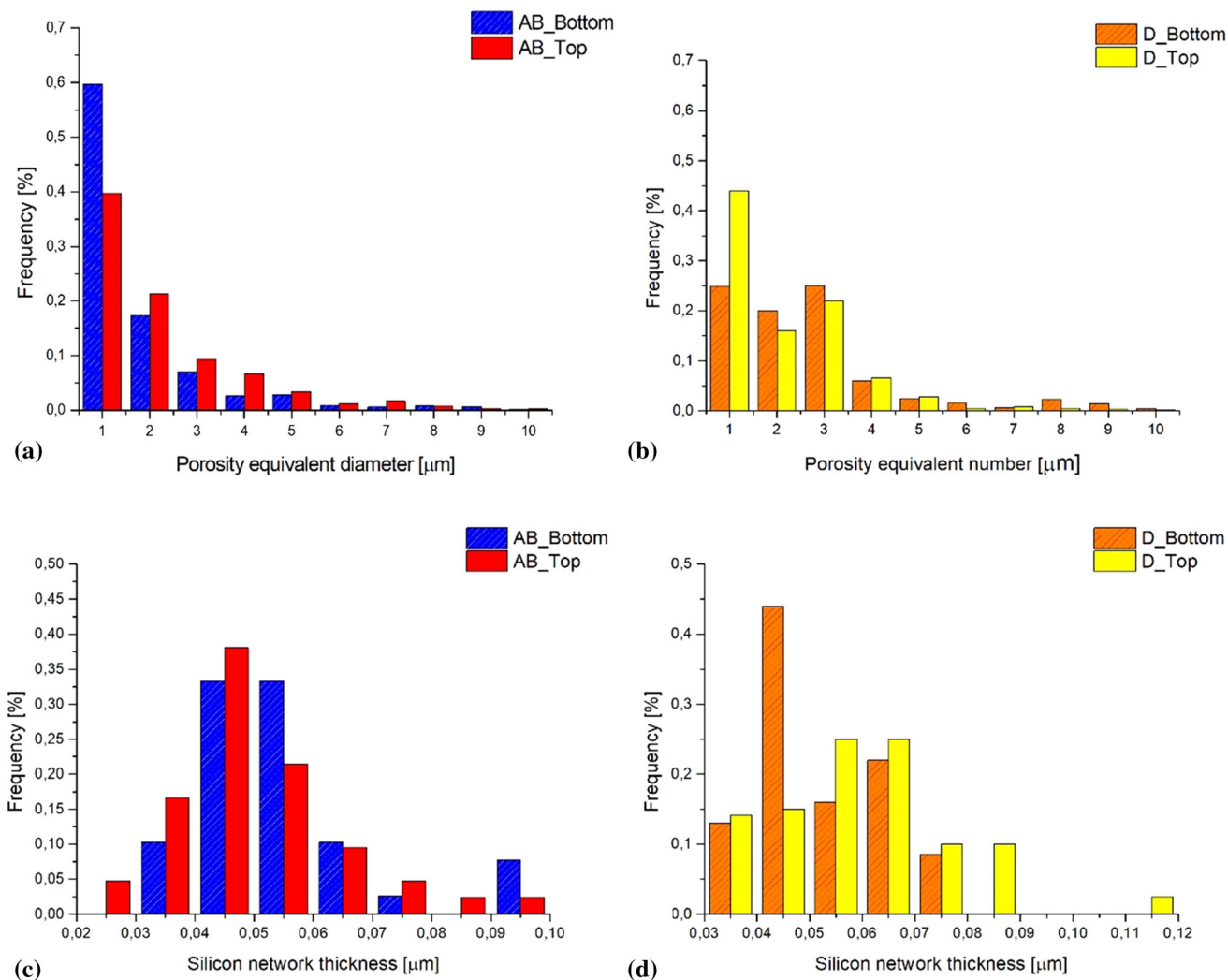


Fig. 5 Statistical distribution of porosity (a, b) and eutectic Silicon network thickness (c, d). (a) Distribution of porosity for AB samples, top and bottom; (b) Distribution of porosity for D samples, top and bottom; (c) Distribution of Si eutectic for AB samples; (d) Distribution of Si eutectic for D samples

Considering the single laser case (D-bottom) in Fig. 5(b), the bottom samples are characterized by 25% of porosity with equivalent diameter smaller than 1 μm, whereas 20% of the pores have diameter in the 1-2 μm range and 25% have a diameter between 2 and 3 μm. The density is 99.0%. As regards the top samples, pores with an equivalent diameter lower than 1 μm account for 45% of the overall porosity; this decreases to 17% and increases again to 22% for the diameter ranges 1-2 μm and 2-3 μm, respectively. The density is 98.5%.

The frequency of pores with equivalent diameter greater than 3 μm tends to 0 both for single and overlapping samples. However, it is possible to observe that the multi-laser case has the highest frequency of smaller pores, as also reported by Li et al. (Ref 6). Moreover, bottom samples show slightly lower porosity than top samples as also reported by (Ref 29); at the same time, in the bottom section there is a higher frequency of small pores (equivalent diameter < 1 μm) than at the top one. As regards the reported values, Aboulkhair et al. (Ref 22) and Buchbinder et al. (Ref 5) suggested a modification of scan strategy and an increase in laser power up to 1 kW, respectively, to increase density. Moreover, the density of as-built AlSi10Mg

SLMed samples was between 95.3% and 99.9%, as reported by Lam et al. (Ref 9).

In the as-built conditions, very fine eutectic silicon is found at the border of α-grains, as shown in high magnification SEM micrographs of Fig. 3. In detail, the average eutectic thickness ranges from 0.045 to 0.065 μm in both kinds of samples (SL and ML) with a standard deviation of 0.020 μm as shown in Fig. 5(c) and (d). Considering such small thickness and the error associated with the measurements, the statistical distributions are similar at the top and bottom in the single and overlapping laser samples. So, in terms of eutectic Si distributions, there are no great microstructural variations in relation to machine setup (single or multi-laser) comparing AB and D bars, as also reported by Zhang et al. (Ref 24). It is inferred that pre-heating the platform at 150 °C does not induce a significant coarsening of eutectic Si. A higher platform temperature, on the other hand, could have caused coarsening of eutectic Si, as reported by Fiegl et al. (Ref 30) and Buchbinder et al. (Ref 31) through experiments with a platform heated at 200 and 250 °C.

Analysis of XRD patterns performed on top and bottom SL samples (Fig. 6) confirms that there are no significant differences in terms of structure. The Mg₂Si phase was detected

through a weak peak at an angle (2θ) of 40.4° in both patterns as reported by (Ref 7, 9).

Figure 7 illustrates the microstructural differences inside the α -grains of top (Fig. 7a and b) and bottom regions (Fig. 7c and d) of the billets, in single (left column) and multi-laser samples (right column).

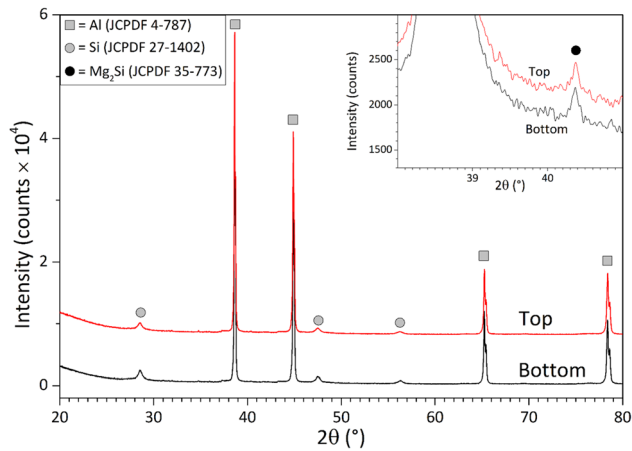


Fig. 6 XRD patterns of the AlSi10Mg top and bottom samples in as-built condition. The inset shows a high-definition pattern acquired around the main peak of Mg_2Si

There are small precipitates phase inside α -Al grains at the bottom (Fig. 7c and d), while precipitates are not visible at the top section (Fig. 7a and b) at the magnification of 80 kX. Higher-resolution views (Fig. 8) at 100 kX clarify that fine, sub-micrometer precipitates (arrows) do exist in both bottom (a) and top (b) samples, but they are more numerous in the former (Fig. 8a). However, it should be remarked that the amount of precipitates is not fully homogeneous: in both areas, the amount of precipitates varies among different grains, probably because of slight differences in thermal history, e.g., among center, coarse zone and HAZ as discussed previously. Considering two different studies of Kim et al. (Ref 32) and Hadadzadeh et al. (Ref 18), the fine precipitates visible within the α -Al grains can be both Si precipitates and Mg_2Si phases; so, this condition represents an additional strengthening of the matrix. All of these are also in agreement with the researchers reported by R. Casati et al. (Ref 15) and Li et al. (Ref 16). In this context, Y. Ji et al. (Ref 33) have demonstrated that the SLM process creates a supersaturated solid solution (SSS) of Si in α -Al matrix due to the solidification process of molten pool. As matter of fact, the high cooling rate (10^6 - 10^8 K/s) reduces quantity of Si rejected into the liquid. With the successive scanned layers, the Si particles precipitate and grow in the previous solidified layer due to the high temperature that is generated (Ref 33-35). T. Kimura et al. (Ref 34) reported the same scenario with a SSS formed by Si and Mg solvents.

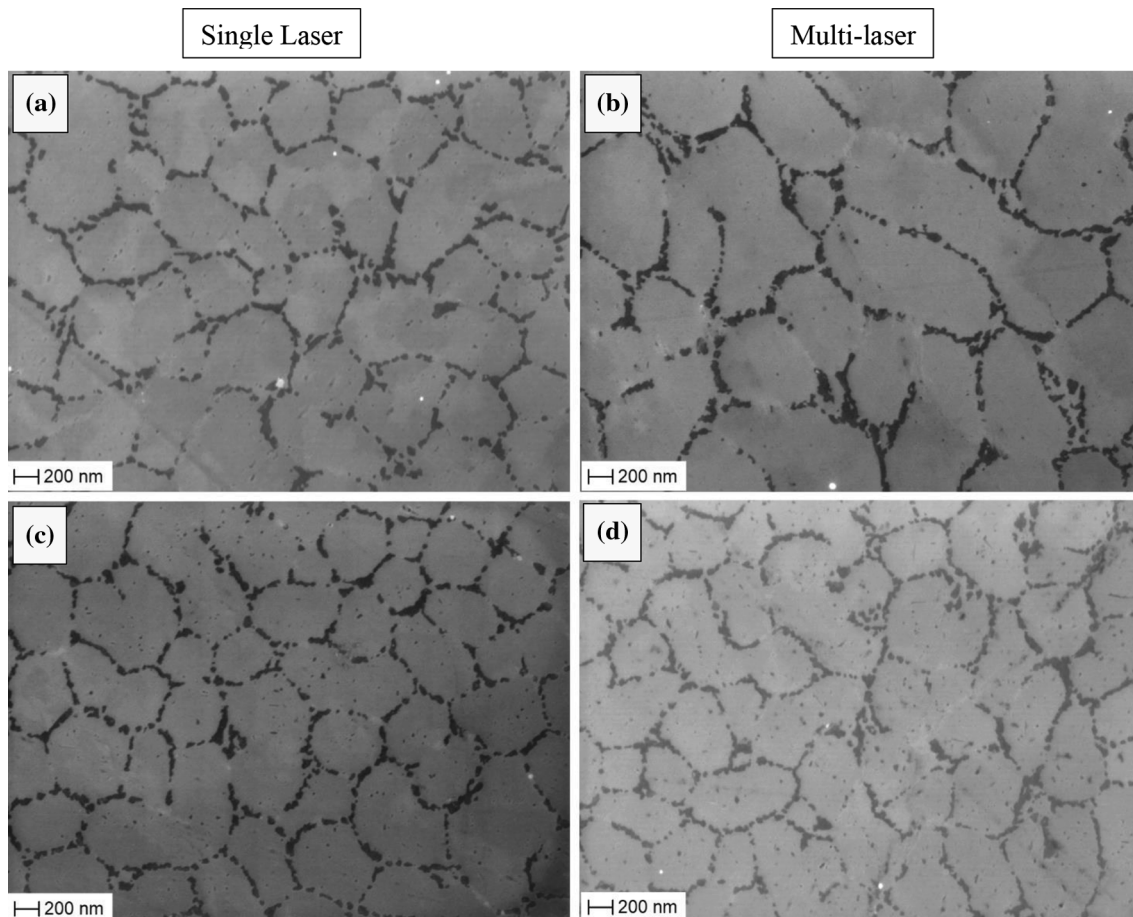


Fig. 7 SEM micrographs of the top regions (a, b) and bottom regions (c, d) of the bars for single laser (a, c) and multi-laser (b, d) samples, respectively

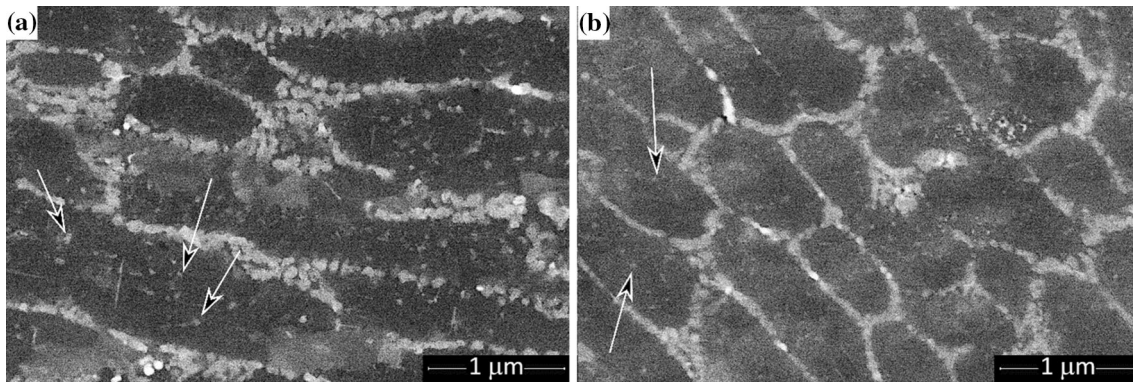


Fig. 8 High-resolution SEM micrographs of the bottom (a) and top (b) regions of the single laser sample. Arrows indicate some nanosized Si within the α -Al grains.

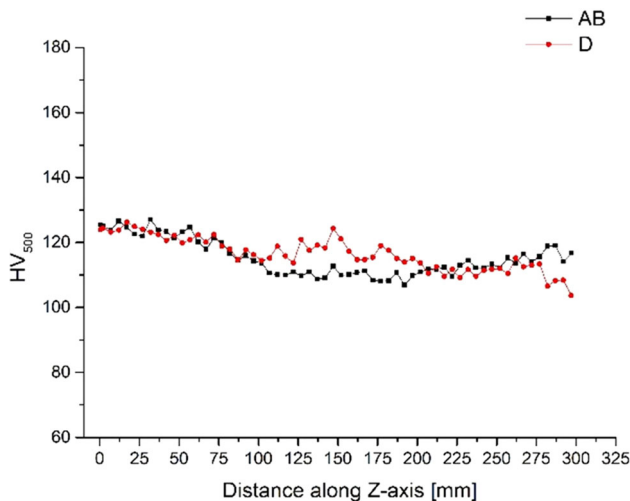


Fig. 9 Microhardness measured along the build (Z) axis for single laser samples (D) and multi-laser samples (AB)

Figure 9 shows the Vickers microhardness measured along the build axis (or Z-axis) of the two bars. Vickers microhardness is higher at the bottom of the bar (~ 125 HV at 0-30 mm distance from the bottom for both bars), but at the maximum height (300 mm), it decreases to 110 HV and 103 HV, respectively, for AB and D bars. In terms of time and according to HV values reported in Fig. 9, HV decreases by 12% and 16% for the single and multi-laser samples, respectively, in 40 h (i.e., the job duration time) during exposure at 150 °C (platform temperature).

The tensile properties measured in samples machined at different heights of the bar (according to Fig. 1a) are illustrated in Fig. 10(a) and (b), as a function of the distance from the platform (distance along Z-axis). The yield strength and the UTS decrease in samples extracted at higher Z, ranging from 290 to 220 MPa and from 440 to 360 MPa, respectively, for the Single laser case. For the multi-laser case, both $\sigma_{0.02}$ and UTS vary from 300 to 190 MPa and from 445 to 345 MPa, respectively. The greatest variation was, therefore, obtained in multi-laser samples (+ 110 MPa for yield strength and + 100 MPa for UTS), compared to the variations obtained for single laser samples, as reported in Table 2. The % engineering elongation, ϵ , shows average values of (7 ± 1) % in both kinds

of samples and over the entire 300 mm-long investigation region along the Z-axis (Fig. 10). Unlike tensile strength, ductility is not affected by increasing distance along the build axis.

Hardness and tensile strength values are closely related to precipitation strengthening phenomena depending on distance from the heated platform as reported in Fig. 7 and 8 and by (Ref 7, 8, 9). In fact, there is a difference between the top and bottom samples in terms of intra-granular precipitates (Si or Mg_2Si phase), as explained previously. This can be regarded as an aging effect due to prolonged exposure to 150 °C. Yang et al. (Ref 36) confirmed that Mg_2Si phase induces a little strengthening at 160 °C for 8h. At the top of Z-axis, i.e., farther away from the heated platform, tensile strength and HV are lower because the matrix contains fewer precipitates. Therefore, it is mainly hardened by solid solution, which is a less effective mechanism than precipitation strengthening. The slight increase in strength (+ 17 MPa for SL case and + 27 MPa for ML case) of the last top samples (Fig. 10) can be attributable to lattice distortion due to Si dispersed in α -Al matrix during SLM process as previously reported (Ref 15, 24, 37). In fact, these samples are not affected by build platform which induces a stress relaxation and/or an overaging, as reported by (Ref 15, 16, 38).

The smaller decline of strengths along the Z-axis in the SL samples compared to ML samples could perhaps be also attributable to lower coarsening of the microstructure due to lower heat input. Anyway, the effect is barely visible by SEM (Fig. 7). In fact, mechanical properties and microstructure are largely comparable between SL and ML samples. In this context, the ML samples are affected by a greater amount of thermal energy than SL samples due to re-melting or partial re-melting of solidified tracks (Ref 15, 39). This situation induces a decrease in anisotropy that characterized the as-built samples; in fact, the thermal gradient induces a $\langle 100 \rangle$ texture orientation of microstructure along build direction, as reported by D. Dai et al. (Ref 35) and Guan et al. (Ref 39). Similarly, C. Zhang et al. (Ref 24) show a greater isotropy for the overlap samples (18.3% of the area) than single laser samples (12.6%). So, also considering the effect of build platform as previously reported, it can be explained how ML samples have a greater loss in strength than SL samples in the middle part of two bars printed. Therefore, in the following paragraphs, only the results of single laser samples will be considered.

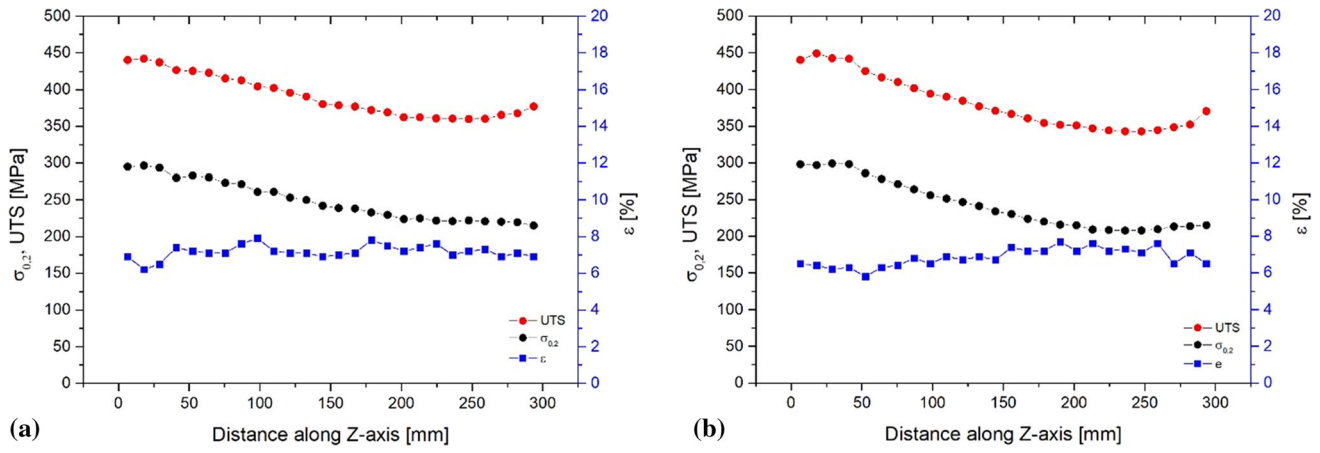


Fig. 10 Tensile properties measured as a function of the distance from the bottom region for (a) multi-laser laser samples and (b) single laser samples

Table 2 Variation of the mechanical properties of AlSi10Mg samples for the single laser case and multi-laser case

	Variation from bottom to top					
	Absolute differences			Relative change		
	$\Delta\sigma_{0.2}$	Δ UTS	$\Delta\epsilon$	$\Delta\sigma_{0.2}$	Δ UTS	$\Delta\epsilon$
Sample AB: Multi-laser	110 MPa	100 MPa	- 0.9 %	- 37%	- 22%	+ 14 %
Sample D: Single laser	70 MPa	80 MPa	- 0.8 %	- 24%	- 18%	+ 12 %

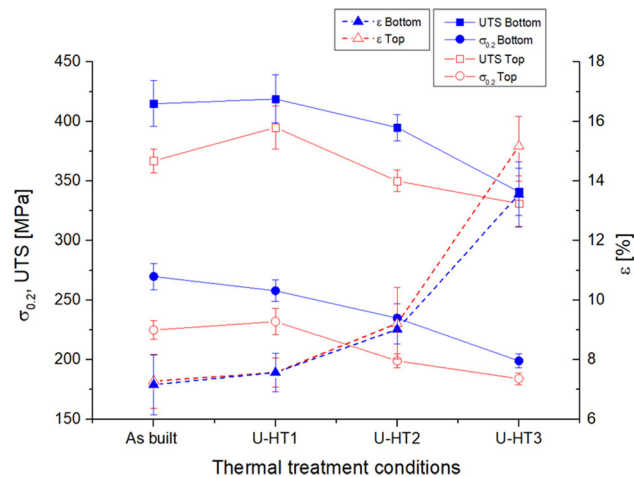


Fig. 11 UTS, yield strength and elongation values of top and bottom AlSi10Mg samples in as-built, U-HT1, U-HT2 and U-HT3 conditions

3.2 Microstructure and Mechanical Properties of Treated AlSi10Mg Samples

Figure 11 presents the trend of tensile strengths and elongations for the AlSi10Mg samples subjected to unconventional treatments at 175, 200 and 225 °C for 6 h, designated as U-HT1, U-HT2 and U-HT3, respectively, for samples at the top

and at the bottom. Values of mechanical properties are also listed in Table 3.

From Fig. 11, the gap reduction of tensile properties between the top and bottom samples is achieved by the U-HT3. In the bottom samples, which had already been aged at 150°C during the build process itself (as explained previously), additional aging due to the treatment at 175 °C has a barely perceivable effect. In the top samples, which were less affected by the pre-heated platform, the aging effect is comparatively more significant. In fact, after the U-HT1 treatment, the top and bottom samples develop comparable microstructures. Both are rich of fine precipitates within the α -Al matrix (Fig. 12a, b). A comparison between Figs. 8(b) and 12(b) particularly highlights the increased amount of fine, intra-granular precipitates in the top sample. The aging condition of both the top and bottom samples has thus become comparable after this heat treatment. On the other hand, the treatment seems not to affect the network of eutectic Si, which remains comparable to the one seen in as-built condition (compare Figs. 12 to 8). Fig. 13 shows that U-HT3 induces an increase in the size of eutectic Si compared to as-built condition. SEM micrographs shown in Fig. 14(a) and (b) highlight the incipient destruction of the Si eutectic network and confirm the coarsening of Si particles compared to Figs. 8 and 12.

After the aging treatment at 225 °C (U-HT3), the UTS and yield strengths have a maximum decrease compared to as-built AlSi10Mg samples for top and bottom regions, while ductility has a maximum increase. In detail, the largest variations occur for the bottom samples and are 24% and 26%, respectively, for

Table 3 Mechanical properties and their variations of top and bottom AlSi10Mg samples depending different heat treatment conditions

HT conditions	UTS, [MPa]		$\sigma_{0.02}$, [MPa]		ϵ , [%]	
	Top	Bottom	Top	Bottom	Top	Bottom
As-built	367 ± 10	415 ± 19	225 ± 8	270 ± 11	7.3 ± 0.7	7.2 ± 0.6
U-HT1	396 ± 18	419 ± 16	232 ± 11	258 ± 9	7.6 ± 0.6	7.6 ± 0.4
U-HT2	350 ± 9	395 ± 11	199 ± 6	235 ± 12	9.2 ± 0.5	9.0 ± 1.0
U-HT3	331 ± 19	341 ± 15	184 ± 5	199 ± 6	15.2 ± 1.0	13.6 ± 1.1

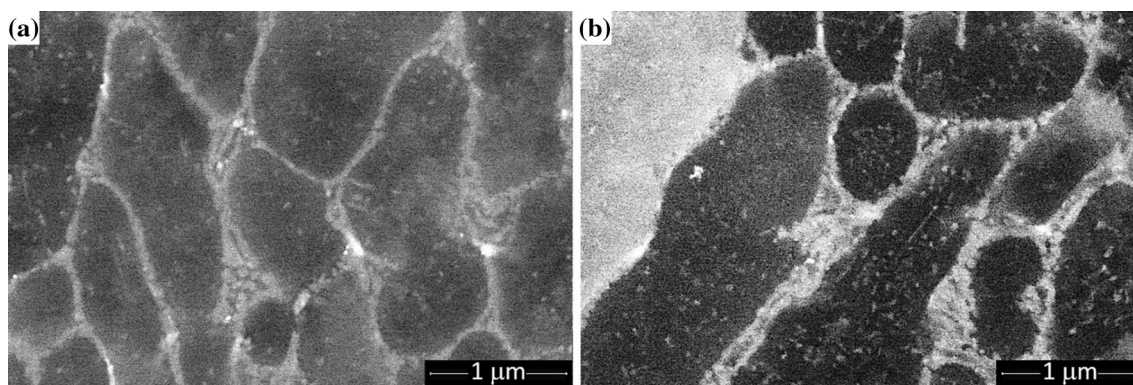


Fig. 12 High-resolution SEM micrographs of the bottom (a) and top (b) AlSi10Mg samples in U-HT1 condition

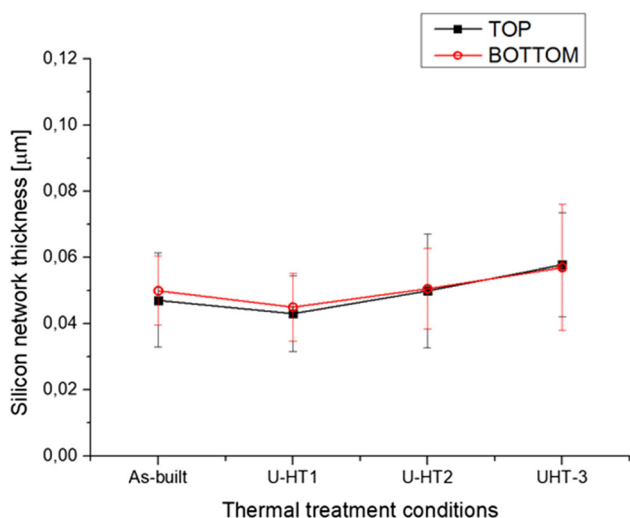


Fig. 13 Average values of Si eutectic thickness measured in as-built condition and different heat treatments

UTS and $\sigma_{0.02}$. Fiocchi et al. (Ref 14) and Mertens et al. (Ref 40) reported comparable results.

Consistently, XRD patterns in Fig. 15(a), (b) and (c) show that the Si peaks become somewhat more intense and narrower after U-HT3 treatment, compared to the as-built condition, which confirms the coarsening of Si. Further, the relative intensity of the different diffraction peaks of α -Al changes after the U-HT3 treatment: the (200) peak at 44.7° becomes more

intense than the (111) peak at 38.5°. This indicates that the α -Al phase is undergoing a change in crystal orientation.

The greatest UTS loss of 74 MPa is, therefore, explained by the combined effects of coarsening of the Si precipitates and interruption of Si eutectic network. The latter phenomenon allows easier movement of dislocations through the neighboring α -Al grains: dislocations are less likely to interact with coarser eutectic Si. Consequently, the strength needed to break the tensile specimen is also reduced; in fact, the required energy for plastic deformation must not be dissipated in the deformation of eutectic Si as reported by (Ref 32).

Due to such major microstructural re-arrangement, the values of tensile strengths become completely comparable between top and bottom samples. Any difference between the aging conditions of top and bottom after the build process is indeed lost through the alterations caused by the U-HT3 treatment. As regards the ductility, the results obtained on the U-HT3 samples can be regarded as optimal values, when compared both to the other samples tested within the present work (as shown in Table 3) and to literature data pertaining to analogous thermal treatment conditions (Ref 6, 14, 30, 41).

The U-HT2 condition, on the other hand, seems to provide an optimum compromise between retaining the mechanical properties and providing acceptable values of elongation, although the effect of the distance from the build platform is retained.

This compromise is achieved as the unconventional heat treatment causes a slight increase in the size of eutectic Si (Fig. 13), as well as a slight coarsening effect on the precipitates within α -Al grains (Fig. 14a, c), but it does not cause a destruction of the Si eutectic network (Fig. 14a, c), compared to the as-built condition (compare to Fig. 8).

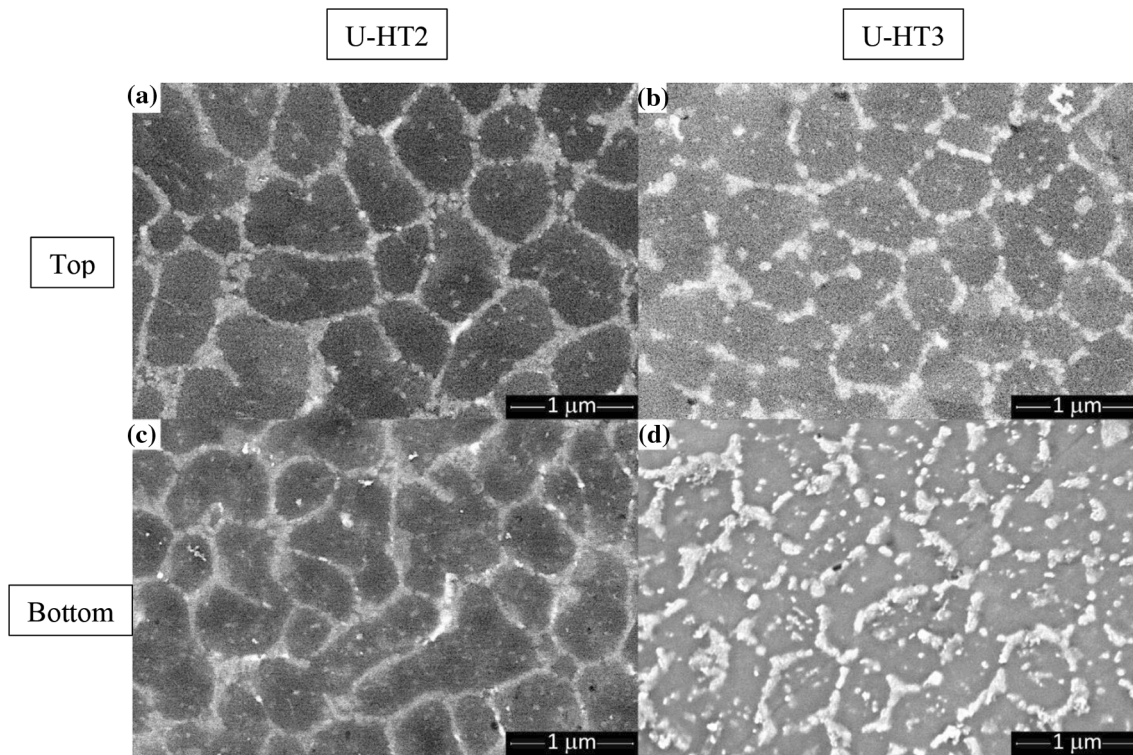


Fig. 14 High-resolution SEM micrographs of the top regions (a, b) and bottom regions (c, d) of the bars, respectively, for U-HT2 (a, c) and U-HT3 (b, d) conditions

4. Conclusions

In summary, the effects of distance from the pre-heated build platform on SLMed AlSi10Mg samples processed by single and multi-laser (SL, ML, respectively) scanning methods were studied. All of these were analyzed in as-built condition and after unconventional heat treatments (U-HTs). The following conclusions have been drawn:

1. An ultrafine and inhomogeneous microstructure was detected in as-built samples by SEM micrographs and XRD analysis. It is characterized by α -Al grains with a network of eutectic Si, and nanosized intra-granular precipitates that likely consist of Si and Mg_2Si phases. There is no substantial difference either between SL and ML or between top and bottom samples in terms of eutectic Si thickness. Proximity to the pre-heated build platform, therefore, does not induce coarsening of eutectic Si. In fact, the range is from $0.045 \mu m$ to $0.065 \mu m$ with a standard deviation of $0.020 \mu m$. However, the SL samples show a lower density than ML samples; furthermore, the porosity decreases from top to bottom samples. Bottom samples also contain greater amounts of intra-granular precipitates.
2. Due to these microstructural differences, the tensile strength and Vickers microhardness decrease linearly as the height increases along the Z-axis for as-built samples. The greatest loss of mechanical properties was achieved

for the ML samples. In detail, HV decreases by 12% and 16% for SL and ML samples, respectively. The yield strength and UTS decrease by about 25% and 18%, respectively, for the SL case, about 35% and 22%, respectively, for the ML case.

3. Unconventional heat treatments with suitably adjusted temperature can provide an optimal combination between strength and ductility. Starting from the highly metastable microstructure of the as-built samples, the aging induced by such heat treatments causes a progressive re-arrangement of the Si network and further intra-granular precipitation. A treatment at $200 \text{ }^\circ\text{C}$, in particular, causes slight rounding and coarsening of Si to yield improved ductility, but still it retains high mechanical strength.
4. The effect induced by the pre-heated platform along the Z-axis was reduced by unconventional heat treatments at $175 \text{ }^\circ\text{C}$ (U-HT1) and $225 \text{ }^\circ\text{C}$ (U-HT3). In the first case, this is due to the aging treatment induced on the “top” samples, which makes them similar to the “bottom” samples that had already been aged by prolonged proximity to the build platform during the SLM process. The second case is characterized by coarsening of both intra-granular precipitates and eutectic Si, and by destruction of the eutectic Si network, which levels out the properties in all areas of the sample. The treatment at $200 \text{ }^\circ\text{C}$ (U-HT2), on the other hand, retains the mechanical properties’ gradient along the Z-axis.

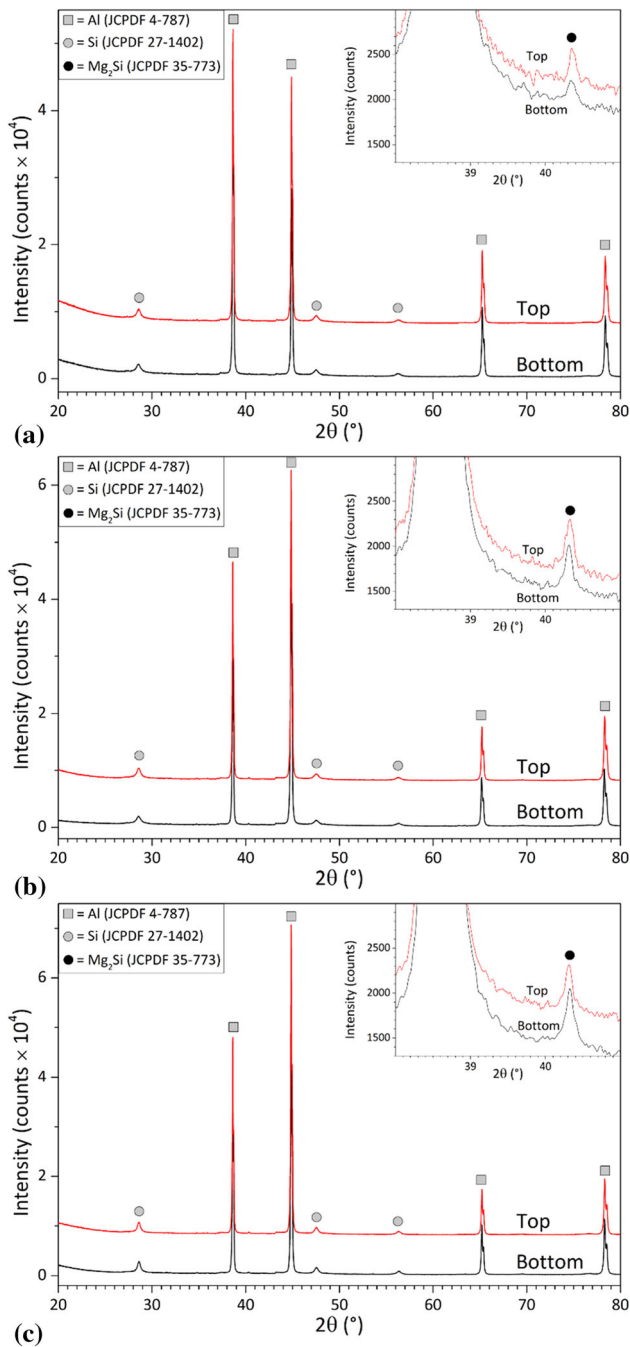


Fig. 15 XRD patterns for AlSi10Mg top and bottom samples in U-HT1 (a), U-HT2 (b) and U-HT3 (c) conditions. Insets show high-definition patterns acquired around the main peak of Mg₂Si

Acknowledgments

The authors would like to thank Ing. Federica Savo for assistance with sample preparation for SEM analyses and Beam-It (Fornovo di Taro (PR-Italy)) for material supply.

Funding

Open access funding provided by Università degli Studi di Parma within the CRUI-CARE Agreement..

Open Access

This article is licensed under a Creative Commons Attribution 4.0 International License, which permits use, sharing, adaptation, distribution and reproduction in any medium or format, as long as you give appropriate credit to the original author(s) and the source, provide a link to the Creative Commons licence, and indicate if changes were made. The images or other third party material in this article are included in the article's Creative Commons licence, unless indicated otherwise in a credit line to the material. If material is not included in the article's Creative Commons licence and your intended use is not permitted by statutory regulation or exceeds the permitted use, you will need to obtain permission directly from the copyright holder. To view a copy of this licence, visit <http://creativecommons.org/licenses/by/4.0/>.

References

1. G. Kasperovich and J. Hausmann, Improvement of Fatigue Resistance and Ductility of Ti6Al4V Processed by Selective Laser Melting, *J. Mater. Process Technol.*, 2015, **220**, p 202–214
2. Y. Liu, Z. Liu, Y. Jiang, G. Wang, Y. Yang and L. Zhang, Gradient in Microstructure and Mechanical Properties of Selective Laser Melted AlSi10Mg, *J. Alloys Compd.*, 2018, **735**, p 1414–1421
3. N. Aboulkhair, I. Maskery, C. Tuck, I. Ashcroft and N. Everitt, The Microstructure and Mechanical Properties of Selective Laser Melted AlSi10Mg: The Effect of Conventional T6-Like Heat Treatment, *Mater. Sci. Eng. A*, 2016, **667**, p 139–143
4. M. Tang and P. Pistorius, Anisotropic Mechanical Behaviour of AlSi10Mg Parts Produced by Selective Laser Melting, *JOM*, 2017, **69**, p 516–552
5. D. Buchbinder, H. Schleifenbaum, S. Heidrick, W. Meines and J. Bueltmann, High Power Selective Laser Melting (HP SLM) of Aluminium Part, *Phys. Procedia*, 2011, **12**, p 271–278
6. Z. Li, Z. Kuai, P. Bai, Y. Nie, G. Fu, W. Liu and S. Yang, Microstructure and Tensile Properties of AlSi10Mg Alloy Manufactured by Multi-Laser Beam Selective Laser Melting (SLM), *Metals*, 2019, **9**, p 1337–1351
7. A. Maamoun, M. Elbestawi, G. Dosbaeva and S. Veldhuis, Thermal Post Processing of AlSi10Mg Parts Produced by Selective Laser Melting Using Recycled Powder, *Addit. Manuf.*, 2018, **21**, p 234–247
8. K. Prashanth and J. Eckert, Formation of Metastable Cellular Microstructures in Selective Laser Melted Alloys, *Alloys Compd.*, 2016, **707**, p 26–34
9. L. Lam, D. Zhang, Z. Liu and C. Chua, Phase Analysis Microstructure Characterization of AlSi10Mg Parts Produced by Selective Laser Melting, *Virtual Phys. Prototyp.*, 2015, **10**, p 207–215
10. E. Brandl, U. Heckenberger, V. Holzinger and D. Buchbinder, Additive Manufactured AlSi10Mg Samples Using Selective Laser Melting: Microstructure, High Cycle Fatigue, and Fracture Behavior, *Mater. Des.*, 2012, **34**, p 159–169
11. K. Guan, Z. Wang, M. Gao, X. Li and X. Zeng, Effects of Processing Parameters on Tensile Properties of Selective Laser Melted 304 Stainless Steel, *Mater. Des.*, 2013, **50**, p 581–586
12. A. Popovich, V. Sufiarov, I. Polozov, E. Borisov, D. Masaylo and A. Orlov, Microstructure and Mechanical Properties of Additive Manufactured Copper Alloys, *Mater. Lett.*, 2016, **179**, p 38–41
13. K. Prashanth, S. Scudino, H. Klauss, K. Sureddi, L. Loeber, Z. Wang, A. Chaubey, U. Kuehn and J. Eckert, Microstructure and Mechanical Properties of Al-12Si Produced by Selective Laser Melting: Effect of Heat Treatment, *Mater. Sci. Eng. A*, 2014, **590**, p 153–160
14. J. Fioocchi, A. Tuissi, P. Bassani and C. Biffi, Low Temperature Annealing Dedicated to AlSi10Mg Selective Laser Melting Products, *J. Alloys Compd.*, 2017, **695**, p 3402–3409
15. R. Casati, M. Nasab, M. Coduri, V. Tirelli and M. Vedani, Effect of Platform Pre-Heating and Thermal Treatments Strategy on Properties of AlSi10Mg Alloy Processed by Selective Laser Melting, *Metals*, 2018, **8**, p 954–966
16. W. Li, S. Li, J. Liu, A. Zhang, Y. Zhou, Q. Wei, C. Yan and Y. Shi, Effect of Heat Treatments on AlSi10Mg Alloy Fabricated by Selective

- Laser Melting: Microstructure Evolution, Mechanical Properties and Fracture Mechanism, *Mater. Sci. Eng. A*, 2016, **633**, p 116–125
17. N. Takata, H. Kodaira, K. Sekizawa, A. Suzuki and M. Kobashi, Change in Microstructure of Selectively Laser Melted AlSi10Mg Alloy with Heat Treatments, *Mater. Sci. Eng. A*, 2017, **704**, p 218–228
 18. A. Hadadzadeh, B. Amirkhiz and M. Mohammadi, Contribution of Mg₂Si Precipitates to the Strength of Direct Metal Laser Sintered AlSi10Mg, *Mater. Sci. Eng. A*, 2019, **739**, p 295–300
 19. V. Fallah, A. Korinek, N. Ofori-Opoku, B. Raesinia, M. Gallerneault, N. Provatas and S. Esmaceli, Atomic-Scale Pathway of Early-Stage Precipitation in Al-Mg-Si Alloys, *Acta Mater.*, 2015, **82**, p 457–467
 20. M.M. Sistiaga, R. Martens, B. Vrancken, X. Wang, B.V. Hooreweder, J. Kruth and J.V. Humbeeck, Changing the Alloy Composition of Al7075 for Better Processability by Selective Laser Melting, *J. Mater. Process. Technol.*, 2016, **238**, p 437–445
 21. L. Zhou, A. Metha, E. Schulz, B. McWilliams, K. Cho and Y. Sohn, Microstructure, Precipitates and Hardness of Selectively Laser Melted AlSi10Mg Alloy Before and After Heat Treatment, *Mater. Charact.*, 2018, **143**, p 5–17
 22. N. Aboulkhair, N. Everitt, I. Ashcroft and C. Tuck, Reducing Porosity in AlSi10Mg Parts Processed by Selective Laser Melting, *Sci. Direct*, 2014, **1–4**, p 77–86
 23. W. Pei, W. Zhenying, C. Zhen, L. Junfeng, Z. Shuzhe and D. Jun, Numerical Simulation and Parametric Analysis of Selective Laser Melting Process of AlSi10Mg Powder, *Appl. Phys.*, 2017, **213**, p 540
 24. C. Zhang, H. Zhu, Z. Hu, L. Zhang and X. Zeng, A Comparative Study on Single-Laser and Multi-Laser Selective Laser Melting AlSi10Mg: Defects, Microstructure and Mechanical Properties, *Mater. Sci. Eng. A*, 2019, **746**, p 416–423
 25. M.S. Pham, B. Dovgvy, P.A. Hooper, C.M. Gourlay and A. Piglione, The Role of Side-branching in Microstructure Development in the Laser Powder-Bed Fusion, *Nat. Commun.*, 2020, **11**, p 749
 26. D. Kong, C. Dong, S. Wei, X. Ni, L. Zhang, R. Li, L. Wang, C. Man and X. Li, About Metastable Cellular Structure in Additively Manufactured Austenitic Stainless Steels, *Add. Man.*, 2021, **38**, p 101804
 27. F. Yan, W. Xiong and E.J. Faierson, Grain Structure Control of Additively Manufactured Metallic Materials, *Materials*, 2017, **10**(11), p 1260–1271
 28. Y. Wang, C. Yu, L. Xing, K. Li, J. Chen, W. Liu, J. Ma and Z. Shen, Grain Structure and Texture of SLM Single Laser, *J. Mater. Proc. Technol.*, 2020, **281**, p 116591
 29. B. Liu, Z. Kuai, Z. Li, J. Tong, P. Bai, B. Li and Y. Nie, Performance Consistency of AlSi10Mg Alloy Manufactured by Simulating Multi Laser Beam Selective Laser Melting (SLM): Microstructures and Mechanical Properties, *Materials*, 2018, **11**, p 2354–2372
 30. T. Fiegel, M. Franke and C. Koerner, Impact of Build Envelope on the Properties of Additive Manufactured Parts from AlSi10Mg, *Opt. Laser Technol.*, 2019, **11**, p 51–57
 31. D. Buchbinder, W. Meiners, N. Pirch, K. Wissenbach and J. Schrage, Investigation on reducing Distortion by Preheating During Manufacture of Aluminum Components Using Selective Laser Melting, *J. Laser Appl.*, 2014, **26**, p 012004
 32. D. Kim, J. Hwang, E. Kim, Y. Heo, W. Woo and S. Choi, Evaluation of the Stress-Strain Relationship of Constituent Phases in AlSi10Mg Alloy Produced by Selective Laser Melting Using Crystal Plasticity FEM, *J. Alloy. Compd.*, 2017, **714**, p 687–697
 33. Y. Ji, C. Dong, D. Kong and X. Li, Design Materials Based on Simulation Results of Silicon Induced Segregation at AlSi10Mg Interface Fabricated by Selective Laser Melting, *J. Mater. Sci. Technol.*, 2020, **46**, p 145–155
 34. T. Kimura and T. Nakamoto, Microstructures and Mechanical Properties of A356 (AlSi7Mg0.3) Aluminium Alloy Fabricated by Selective Laser Melting, *Mater. Des.*, 2016, **86**, p 1294–1301
 35. D. Dai, D. Gu, R. Poprawe and M. Xia, Influence of Additive Multilayer Feature on Thermodynamics, Stress and Microstructure Development During Laser 3D Printing of Aluminium-Based Material, *Sci. Bull.*, 2017, **62**, p 779–787
 36. K. Yang, P. Rometsch, C. Davies, A. Huang and X. Wu, Effect of Heat Treatment on the Microstructure and Anisotropy in Mechanical Properties of A357 Alloy Produced by Selective Laser Melting, *Mater. Des.*, 2018, **154**, p 257–290
 37. E.A. Jäggle, Z. Sheng, L. Wu, L. Lu, J. Kisse, A. Weisheit and D. Raabe, Prediction Reactions in Age-Hardenable Alloys During Laser Additive Manufacturing, *JOM*, 2016, **68**, p 943–949
 38. A.H. Maamoun, M. Elbestawi, G.K. Dosbaeva and S.C. Veldhuis, Thermal Post-Processing of AlSi10Mg Parts Produced by Selective Laser Melting Using Recycle Powder, *Addit. Manuf.*, 2018, **21**, p 234–247
 39. J. Guan, Y. Jiang, X. Zhang and X. Chong, Microstructural Evolution and EBSD Analysis of AlSi10Mg Alloy Fabricated by Selective Laser Melting, *Mater. Charact.*, 2020, **161**, p 110079
 40. A. Mertens, O. Dedri, D. Reuter, O. Rigo and J. Lecomte-Beckers, Thermal Treatments of AlSi10Mg Processed by Laser Beam Melting, in *Proceedings of the 26th International Solid Freeform Fabrication Symposium* vol. 1 (2015)
 41. C. Zhang, H. Zhu, Y. Qi and X. Zeng, The Effect of Annealing on Microstructure and Mechanical Properties of Selective Laser Melting AlSi10Mg, in *Materials Science and Engineering*, vol. 538 (2019)

Publisher's Note Springer Nature remains neutral with regard to jurisdictional claims in published maps and institutional affiliations.